Stress in the Contorted Nazca Plate Beneath Southern Peru From Local Earthquakes

JOHN F. SCHNEIDER AND I. SELWYN SACKS

Department of Terrestrial Magnetism, Carnegie Institution of Washington

We study earthquake focal mechanisms in a region of highly contorted subducting lithosphere to identify dominant sources of stress in the subduction process. We observe a stress pattern in the contorted Nazca plate beneath southern Peru from an analysis of hypocentral trend and focal mechanisms of intermediate-depth earthquakes. Expanding on previous studies, we examine the hypocentral trend using 1673 of 2178 well-located local events from the nine-station Arequipa network. The dip of the plate beneath southern Peru averages 25°– 30° from 25- to 100-km depth. Below this depth there is an 80- to 100-km-wide contortion between a zone of increasing dip (convex) to the southeast and a flat lying (concave) zone to the northwest. Using more than 6000 P wave first motions of events deeper than 50 km, we derive stress orientations from a moving average of composite focal mechanisms across a 200 by 350 km region including the contortion. The in-plate distribution of tension (T) and compression (P) axes reveals a coherent stress pattern. The trend is most clear beneath south-central Peru (NW section) and below 100-km depth in southernmost Peru (SE section). Both T and P axes tend to be dominantly in plate, especially below 100-km depth. T axes orient toward the contortion in a fan-shaped trend, which suggests that the deepest part of the seismic zone, within the convex SE section, is sinking and pulling the more buoyant NW section. We conclude that from 50- to 200-km depth, slab-pull forces are dominant in the observed stress. Our results suggest that a significant amount of plate extension occurs in this region of intermediate-depth subduction.

INTRODUCTION

The subduction of the Nazca plate beneath western South America serves as a model for the subduction of an oceanic plate beneath a continent. The hypocenter distribution and focal mechanisms of earthquakes within the subducting lithosphere allow us to observe the stress distribution and provide constraints for resolving dominant forces in the subduction process.

The subducting Nazca plate can be divided into a series of segments, each exhibiting a characteristic subduction profile from the distribution of earthquake hypocenters [*Barazangi and Isacks*, 1976, 1979; *Isacks and Barazangi*, 1977] (Figure 1). Beneath southern Peru and northern Chile, the Wadati-Benioff (W-B) zone is well illuminated and dips at an average of 30° to at least 250-km depth. In south-central Peru the subduction profile is initially the same as in southern Peru, but at ~ 100-km depth the plate subducts horizontally beneath the continent. Between these regions is a continuous contortion at least 80 km wide [*Hasegawa and Sacks*, 1981; *Bevis and Isacks*, 1984; *Boyd et al.*, 1984; *Grange et al.*, 1984]. In central Peru the subduction geometry is less clear due to the paucity of seismicity; two models for the subduction geometry have been proposed. One model [e.g., *Barazangi and Isacks*, 1976, 1979], based largely on the distribution of selected teleseismically determined earthquake hypocenters, suggests that the W-B zone dips gradually at about 10° to 700 km from the trench. The other model [e.g., *Snoke et al.*, 1977, 1979; *Hasegawa and Sacks*, 1981], based principally on the analysis of ScSp wave conversions at the top of the subducting lithosphere, differs in defining the initial plate dip to be 30° to 100-km depth. All authors agree, however, that there are no major lateral changes in

the subduction geometry for several hundred kilometers either north or south along the trench strike outside of the contortion in southern Peru.

The contortion occurs beneath a major bend in the Andes mountains, at the northern terminus of an active line of volcanoes [*Sacks*, 1977; *Barazangi and Isacks*, 1979; *Jordan et al.*, 1983; *Bevis and Isacks*, 1984]. A model constrained by age of the plate, bathymetry, and heat flow indicates that the Nazca plate is nearly neutrally buoyant in this region [*Sacks*, 1983]. Beneath central Peru, the Nazca plate contains the buoyant Nazca Ridge (Figure 1) and subducts immediately beneath the continental lithosphere, while beneath southern Peru the plate subducts more normally into the asthenosphere. Although the net buoyancy is presumed to be strongly affected by the position of the Nazca Ridge, the contortion itself lies 200 km south of the projection of the Nazca Ridge beneath the surface.

Global studies of earthquake focal mechanisms in subduction zones have revealed several different patterns for the observed stress. Whereas deep earthquakes tend to exhibit downdip compression, intermediate-depth earthquakes are not so easily categorized [e.g., *Isacks and Molnar*, 1971; *Fujita and Kanamori*, 1981; *Vassiliou*, 1984]. It has been shown, however, that at least in western South America, intermediate-depth earthquakes tend to exhibit downdip tension [e.g., *Isacks and Molnar*, 1971; *Stauder*, 1973, 1975; *Hasegawa and Sacks*, 1981]. It is apparent that stress in this depth range is controlled in part by the age of the slab and the rate of convergence. For instance, based mainly on observations in South America, young and fast subducting slabs are universally in downdip tension [*Fujita and Kanamori*, 1981]. However, a satisfactory explanation for this phenomenon seems to be lacking. The analysis of earthquake-observed stress within a contorted W-B zone can be used to differentiate between several competing sources of stress. For instance, we wish to determine whether normal subduction processes such as slab sink-
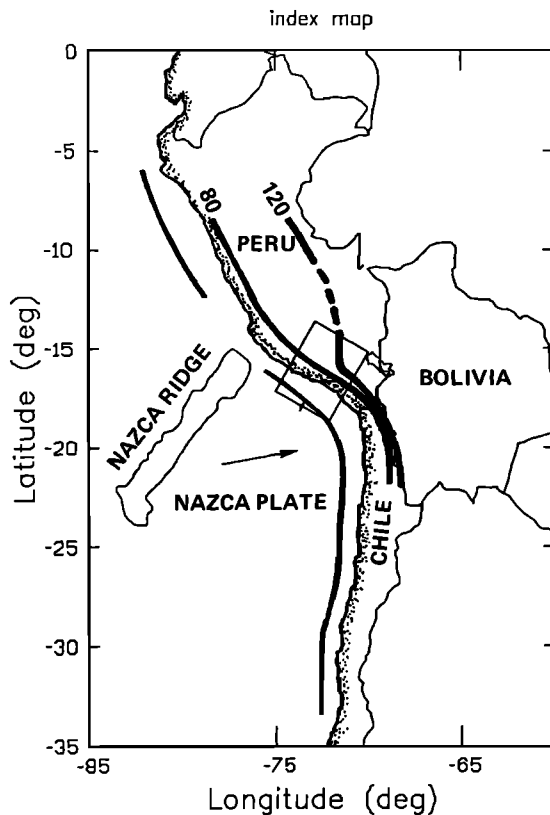
index map

Fig. 1. Tectonic map of western South America. The location of the study area, a 350 by 450 km rectangular region, is shown with respect to the Peru-Chile trench and the Nazca Ridge. The local convergence direction of the Nazca plate relative to the South American plate is indicated as N80E (10 cm/yr; [*Minster and Jordan*, 1978]). Contours indicate depth to the W-B zone (dashed where inferred). The zone of transition between the concave section of the subducting plate to the NW and the convex section to the SE is indicated by the bend in the 120-km depth contour.

ponent, short-period (0.5–8 Hz) seismographs that recorded with pen and ink on revolving drums to a time resolution of 0.1 s. In addition, ARE provided long-period World-Wide Standard Seismograph Network (WWSSN) data and CUS provided three components at short period. While the hypocenter distribution of the 1965 data was discussed previously by *Hasegawa and Sacks* [1981], a more detailed and complete analysis of hypocenters was given by *Boyd et al.* [1984] from the first 32 months of recording. The present study utilizes the Boyd et al. hypocenters, plus new hypocenters derived from the additional 4 months of arrival time data from 1976. An objective set of selection criteria was developed to arrive at a total of 2178 events from the complete 36 months of recording.

The basic method used to locate events is an iterative, least squares procedure that minimizes travel time residuals, solving simultaneously for hypocenter and origin time [*James et al.*, 1969; *Hasegawa and Sacks*, 1981; *Boyd et al.*, 1984]. Events recorded at seven or more stations that satisfy additional selection criteria are defined to be "master" events [e.g., *Evernden*, 1969], from which station corrections are derived. These station corrections are used to locate less constrained (secondary) events in a relative sense [*Hasegawa and Sacks*, 1981; *Boyd et al.*, 1984]. Following *Boyd et al.* [1984], station corrections for each secondary event are distance-weighted functions of the travel time residuals of master events whose epicenters lie within 50 km of the initial secondary-event epicenter. Each secondary event is then relocated using these station corrections.

In locating the remaining 4 months of data from 1976, we calculated station corrections from the same set of 205 master events defined by Boyd et al. from their 32-month data set. We then applied an objective set of sorting criteria to the entire 36 months of data, as outlined in Table 1. Although our guidelines follow very closely those outlined by *Boyd et al.* [1984] for the 32-month data set, differences arise largely in Boyd et al.'s allowances for subjective discrimi-

ing can explain the observed contortion, or whether other anomalous sources of stress related to plate geometry or plate bending might also be important.

The purpose of this paper is to observe patterns of stress in the contorted Nazca plate beneath southern Peru from the analysis of earthquake focal mechanisms of intermediate-depth earthquakes. Using data from a local array, we first examine the trend of earthquake hypocenters and discuss the shape of the W-B zone in the vicinity of the contortion. Then using *P* wave first motions, we generate a stress distribution from a moving average of composite focal mechanisms across the W-B zone. The distribution of tension (*T*) and compression (*P*) axes is expressed relative to the W-B zone shape to reveal a coherent pattern of stress.

HYPOCENTER DATA

Event Locations

The earthquakes analyzed in this study were recorded by the Arequipa network of nine seismograph stations operated by the Characato Observatory of the Universidad Nacional de San Agustin in Arequipa, Peru (Figure 2). The data used in our study come from three 12-month periods in 1965, 1969, and 1975–1976. With the exception of ARE and CUS, the network was comprised of single vertical com-
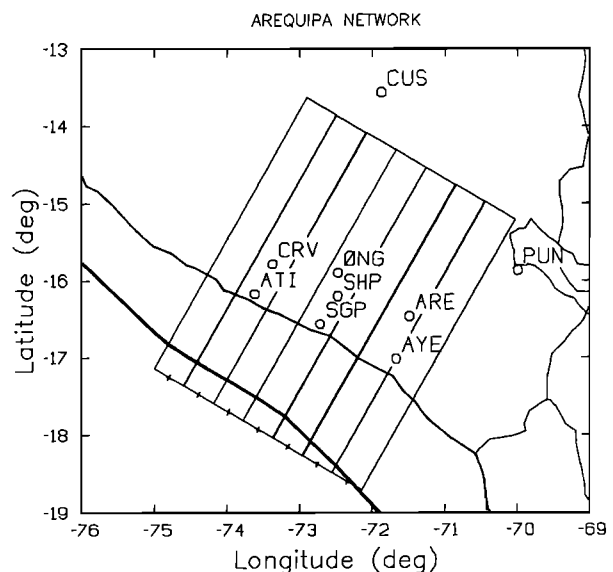

Fig. 2. The Arequipa network of seismograph stations in southern Peru. The nine-station network is shown relative to the study area, which is divided into seven 50-km-wide rectangles. The study area is oriented with the SW edge striking N60W and parallel to the trench.

TABLE 1. Selection Criteria for Earthquake Hypocenters

Symbol in Figures	Depth, km	Rms Resid- ual	P wave Observ- ation	Distance: Depth	A axis, km	Z axis, km	Origin Time, s	No. of Events
Cross	<60	≤1.0	4	≤2.0	≤10.0	≤10.0	≤1.0	168
Diamond	<60	≤1.5	5-6	≤2.0	≤15.0	≤15.0	≤1.5	356
Square	<60	≤2.0	7-9	≤2.0	≤15.0	≤15.0	≤2.0	84
Cross	≥60	≤1.0	4	≤1.0	≤10.0	≤10.0	≤1.0	393
Diamond	≥60	≤1.5	5-6	≤1.0	≤15.0	≤15.0	≤1.5	826
Square	≥60	≤2.0	7-9	≤1.0	≤15.0	≤15.0	≤2.0	349
Master	>50	≤1.0	7-9	≤1.0	≤10.0	≤10.0	≤1.0	205

The Rms residual is of P wave travel times; distance: depth is the ratio of the distance to the nearest station over the event depth; A axis is the major axis of a horizontal error ellipse at 75% confidence for two degrees of freedom (based on the F statistic [Flinn, 1965; Boyd et al., 1984]); Z axis is the depth error at 75% confidence; and the origin time is the error at 75% confidence. The error bounds for master events are only approximate. An additional constraint requires that locations converge monotonically in the iteration procedure.

nation of solution quality. In comparing results, we found that while the new criteria may have eliminated some viable solutions, they also rejected undetected poor solutions (1-2%) and accepted some events (3%) erroneously removed previously. These differences do not significantly alter the observed distribution of hypocenters.

The seismicity region was divided into seven rectangles, each 50 by 450 km (Figure 3), with the SW side aligned approximately parallel to the strike of the trench (N60W). Events in each rectangle are plotted in vertical cross sections taken perpendicular to the trench strike (Figure 4a). There are no significant differences between these cross sections and those presented by Boyd et al. [1984]; however, Boyd et al.'s seismicity projections were bounded along the trench strike approximately by stations AYE and ATI (Figure 2). Thus hypocenters projected in rectangles A and G and half of rectangle F (Figures 3 and 4a) have not been presented previously.

Boyd et al. [1984] demonstrate that the master-event technique reduces the effect of apparent scatter, particularly in deeper events that occur farther inland, and outside the seven coastal stations. Their results are consistent with model simulations of the effect of array configuration and heterogeneities in slab velocity on the apparent W-B zone shape [McLaren and Frohlich, 1985]. For an array configuration dominated by coastal stations, the effect of a high-velocity slab dipping inland is to increase the apparent dip of the W-B zone such that a planar slab would appear convex upward. The effect is minimized for a uniformly distributed array. With respect to the Arequipa network, since the master events require observations from ≥7 of 9 stations, these events are likely to include observations from one or both inland stations (i.e., CUS and/or PUN, Figure 2). Thus the use of master events reduces the relative error due to station bias, producing a more realistic slab shape and thereby emphasizing the concave upward nature of the northwestern portion of the W-B zone.

Wadati-Benioff Zone Shape

We may use the hypocenter distribution to define a shape or surface for the W-B zone beneath southern Peru. If the

hypocenter distribution maintains the same relative location within the plate, then such a surface should be a reasonable representation of the shape of the subducting Nazca plate. Other models of the W-B zone shape have been derived for this same region of southern Peru but from less well-constrained data. Bevis and Isacks [1984], utilizing a surface spherical-harmonic expansion, derived a local model from a small subset of this data set reported on by Hasegawa and Sacks [1981]. Seismicity-depth contours were also empirically defined by Grange et al. [1984] from the hypocentral trend of microseismicity data in this same area.

We utilize a series of one-dimensional cubic splines to approximate a surface defined at discrete intervals on a horizontal (Cartesian) grid. Cubic splines are fit in a least squares sense to a series of vertical cross sections both par-
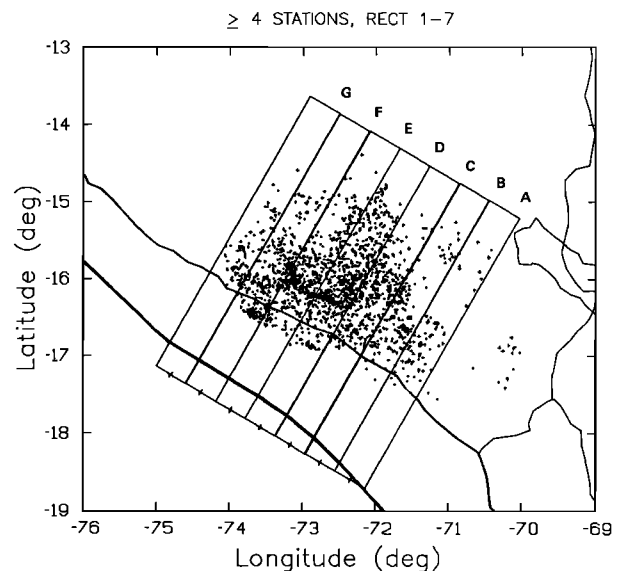

Fig. 3. Plan view of seismicity derived from 36 months of recording from the nine-station Arequipa seismograph network. The 2178 epicenters that satisfy the sorting criteria (Table 1) are plotted. Letters A-G refer to the seven rectangles for which vertical cross sections are projected perpendicular to the trench in Figure 4.
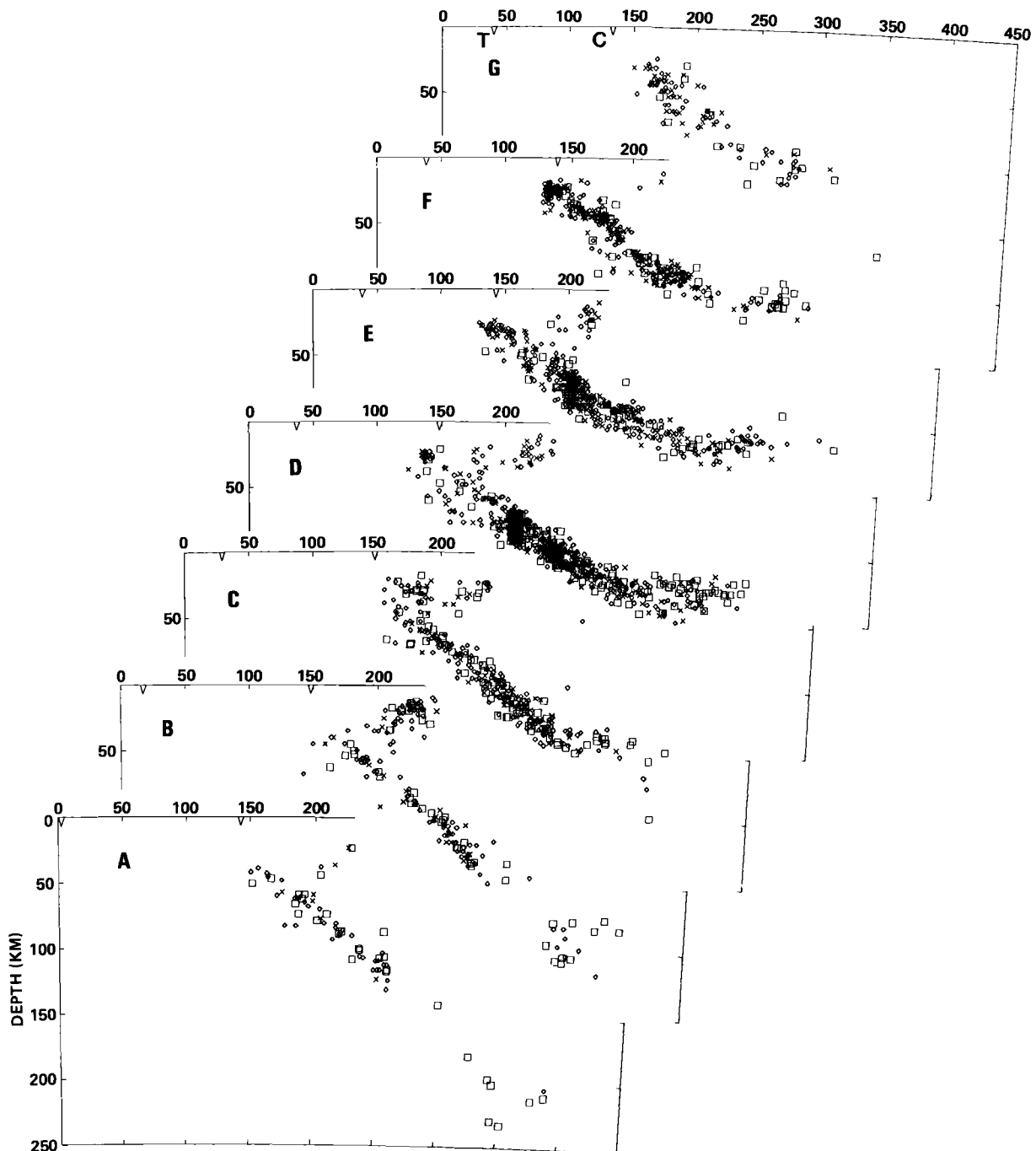
Fig. 4a.　Vertical cross sections of local seismicity from the Arequipa network. The 50-km-wide cross sections are viewed from SE (bottom) to NW (top) looking parallel to the trench (T) and coastline (C) (N60W). Event symbols are defined in Table 1.

allel and perpendicular to the trench strike. Curves fitting through cross sections where the data density is greatest and most uniform are used to partially constrain functions fit through orthogonal sections in order to (1) minimize instabilities where data density is low and (2) to ensure approximate intersection of orthogonal curves. Several criteria are important to define a reasonable surface.

1. No major bends or contortions in the plate are allowed over distances small with respect to the apparent hypocenter thickness (20–30 km). We regard this thickness as an upper bound on relative depth error, and hence as a limit to our resolution of surface smoothness.

2. To minimize the effect of variations in hypocenter

distribution with respect to the Nazca plate geometry, we consider only those events likely to have occurred within the Nazca plate. Thus we consider only events at depths ≥ 50 km, eliminating those events likely to have occurred either at the oceanic-continental plate boundary, or within the overriding continental lithosphere.

3. Because of the uncertainties in relating confidence intervals and numbers of arrival time observations to any realistic location error, we weighted all event locations equally in the least squares minimization process.

4. We constrained all curves fit perpendicular to the trench to intersect the trench at 5-km depth.

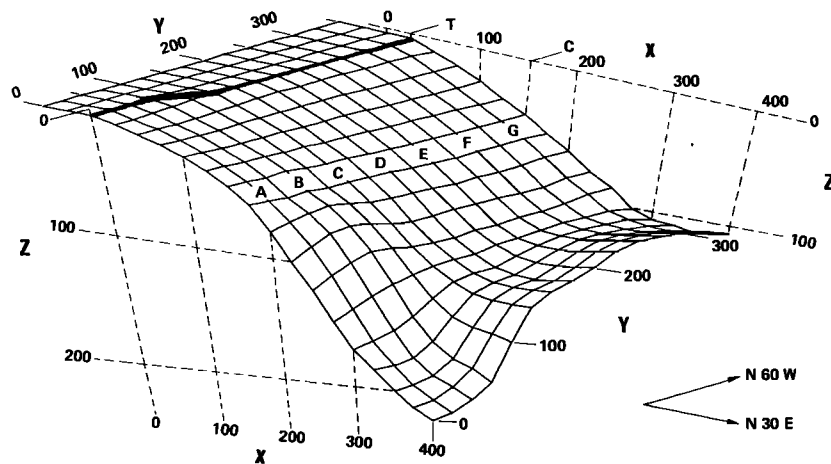The final surface, utilizing 1673 hypocenters, is a two-

Fig. 4b. The W-B zone shape viewed looking N105W, at 45° to the trench (T, dark line). A Cartesian coordinate system is indicated for reference to other figures, with x and y axes perpendicular and parallel to the trench, respectively. Grid points are at 25-km intervals in x and y. Labels A-G refer to the locations of seismicity cross sections (Figure 4a). Below 100-km depth it is useful to refer to the NW portion (far right, sections E-G) as the concave zone, the middle portion (sections C-D) as the contorted zone, and the SE portion (foreground) as the convex zone.

dimensional, horizontal grid defined as a function of depth at 25-km intervals (Figure 4b). This surface approximates the W-B zone shape, indicating that (1) throughout south-central and southern Peru the slab strike remains parallel to the trench at N60W to approximately 80-km depth at 250 km from the trench (the dip averaging 25° from 25- to 80-km depth); (2) beyond 300 km from the trench the NW portion (south-central Peru) of the slab is nearly horizontal at 110-km depth from 300 to at least 400 km from the trench; (3) the SE portion (southern Peru) of the slab maintains a normal profile, with the dip increasing to about 40° between 100- and 220-km depths; and (4) between the NW and SE sections there is a 100-km-wide contortion between 110- and 220-km depths, with local dips of 45° or more to the SE and parallel to the trench.

Our model agrees to first order with local models determined by Bevis and Isacks [1984] and Grange et al. [1984]. However, due to greater data density, our W-B zone shape is better constrained, particularly below 100-km depth. We do not observe a single, well-defined contortion axis extending parallel to the direction of relative plate motion (N80E), as concluded by Grange et al. [1984]. As we shall discuss later, this difference has implications for the interpretation of the stress distribution.

FOCAL MECHANISMS

An analysis of earthquake focal mechanisms, and their correlation with the W-B zone structure, is critical to an understanding of earthquake-related stress and the subduction process. Intermediate-depth earthquakes occur within the plate and are likely to be direct expressions of the stress within the subducting plate. Several authors have investigated focal mechanisms of intermediate-depth events in Peru and northern Chile [Isacks and Molnar, 1971; Stauder, 1973, 1975; Hasegawa and Sacks, 1981; Grange et al., 1984]. A sparse distribution of well-constrained fault plane solutions from teleseismic P and S wave arrivals suggests a general tendency for downdip tension [Isacks and Molnar, 1971; Stauder, 1973, 1975], but does not reveal the complex nature of the subduction process in this region.

Expanding on Stauder's [1975] observations in Peru, Hasegawa and Sacks [1981] used composite focal mechanisms of teleseismic P wave arrivals to demonstrate that the tension axis remains essentially perpendicular to the trench and parallel to the local trend in seismicity, suggesting that the Nazca plate behaves as a stress guide throughout the intermediate-depth zone. While Hasegawa and Sacks [1981] utilize two events and Stauder [1975] presents one focal mechanism (event 24) from within the contortion itself, the information is insufficient to suggest a trend or stress pattern. Grange et al. [1984] present some detail in the vicinity of the contortion in their study of selected focal mechanisms of microearthquakes in southern Peru. They indicate that mechanisms from 40- to 100-km depth are highly variable and do not yield a clear view of their connection to subduction, while events deeper than 100 km exhibit more consistent mechanisms, with tension (T) axes generally horizontal and perpendicular to the seismic depth contours.

The present study of focal mechanisms emphasizes intermediate-depth activity (i.e., >50-km depth) beneath southern Peru to derive a coherent stress pattern from microearthquakes, especially in the vicinity of the W-B zone contortion. Our data consist of P wave first-motion (polarity) readings from the same 36 months of Arequipa network data used to compile hypocenters. From an initial set of more than 12,000 polarity readings, we selected about 6000 readings reported as impulsive and from events satisfying the criteria used for hypocenter sorting (Table 1). These data are divided into overlapping groups by hypocentral region to analyze composite focal mechanisms and to evaluate patterns of earthquake stress. The distribution of tensional (T) and compressional (P) axes across the W-B zone yields a coherent stress pattern that may be interpreted in terms of the mechanics of the subduction process.

Reliability of Polarity Data

Before discussing our analysis procedure, it is important to assess the reliability of our polarity data. However, because there are at most nine polarity readings for any given event, data reliability cannot be determined from local
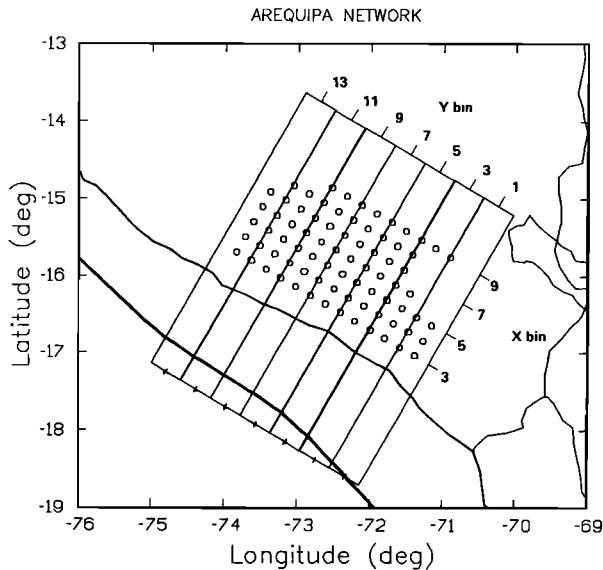
AREQUIPA NETWORK

Fig. 5a

Fig. 5. The array of 78 event bins used for composite focal mechanism solutions. The W-B zone is divided into an array of event bins whose epicenters are centered at 25-km spacings; epicenters (top) and their projections onto the W-B zone surface (bottom) are shown. Each bin is a sphere of 25-km radius and overlaps neighboring bins by ≤25 km. The labeling convention is bin x-y. Events shallower than 50-km depth are not considered in our present analysis, so bins for x = 1, 2 are omitted. Other omissions in the array are for bins having fewer than 10 impulsive polarity readings.

data alone. We can, however, test selected regional events recorded both locally and teleseismically and compare well-constrained mechanisms from single events to readings from Arequipa network stations.

We tested several large, regional events recorded in 1965 and 1969, for which focal mechanisms were determined from teleseismic arrivals by *Isacks and Molnar* [1971] and/or *Stauder* [1973, 1975]. First, as a check on station calibration, we investigated deep events from western South America because such events are most likely to have generated impulsive, direct-wave arrivals at Arequipa network stations. Two deep events, located beneath the Peru-Brazil border (November 3, 1965, 0139 at 9.1° S, 71.4° W at 593-km depth) and beneath northern Argentina (March 5, 1965, 1432 at 27.0° S, 63.3° W at 573-km depth), were recorded

very clearly across the array. The Arequipa net polarities are in complete agreement with well-constrained fault plane solutions [*Isacks and Molnar*, 1971; *Stauder*, 1973, 1975]. In order to verify calibration over time, we divided the data set into three 12-month recording periods and looked at distributions of polarities for various spatial event clusters at each station. Ray paths exhibiting either dominant compression or dilatation in 1965 were compared with similar ray paths in 1969 and 1975–1976. No changes in polarity distribution were observed that would indicate the polarity inversion of any station. We conclude that stations were properly calibrated with respect to polarity for the duration of the data set.

We have also tested the polarity data for reading reliability and internal consistency. Intermediate-depth events occurring within or near the Arequipa network, and having well-constrained hypocenter locations and mechanisms, are subject to similar reading errors as other events used in this study. For a selection of five intermediate-depth events within 10° of the network and recorded by Arequipa network stations, there is a 90% agreement with well-constrained mechanisms of *Isacks and Molnar* [1971] and *Stauder* [1973, 1975]. We evaluated internal data consistency as well by checking events with ≥7 polarity readings from Arequipa network stations alone for consistency with double-couple mechanisms. Based on our findings, we estimate that impulsive *P* wave arrivals are reliable to about an 85–90% level of accuracy.

Composite Focal Spheres

Polarity readings are divided into a series of averaging regions or bins based on hypocenter distribution. We determined the size of each bin and the distribution of bins· to balance the advantages of a wide polarity distribution for constraining mechanisms with the structural scale resolvable from the hypocenter distribution. We established a two-dimensional grid (or array) of points at 25-km intervals in epicenter, with axes parallel and perpendicular to the trench axis (Figure 5a). This interval conforms to our constraints on W-B zone shape. Each point on the grid represents the center of an averaging focal region (or bin), defined as a sphere of 25-km radius and centered within the W-B zone (Figure 5b). Thus there is substantial overlap (i.e., up to 25 km) between adjacent bins. Polarities from each bin are projected onto respective composite focal spheres using the same J-B *P* wave velocity model [*Jeffreys*
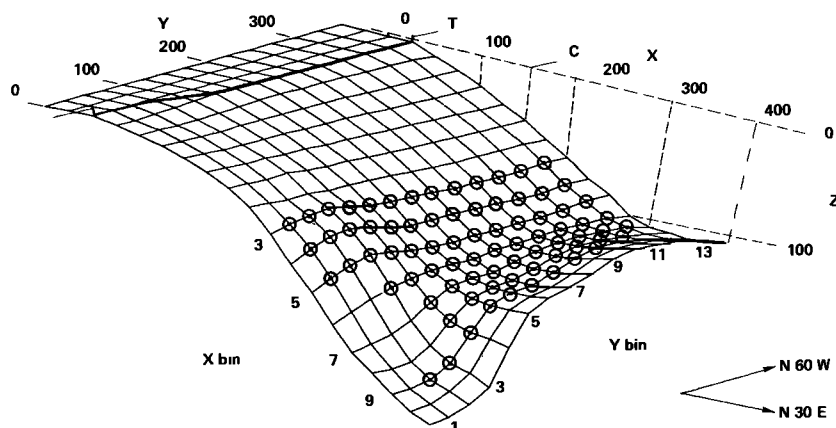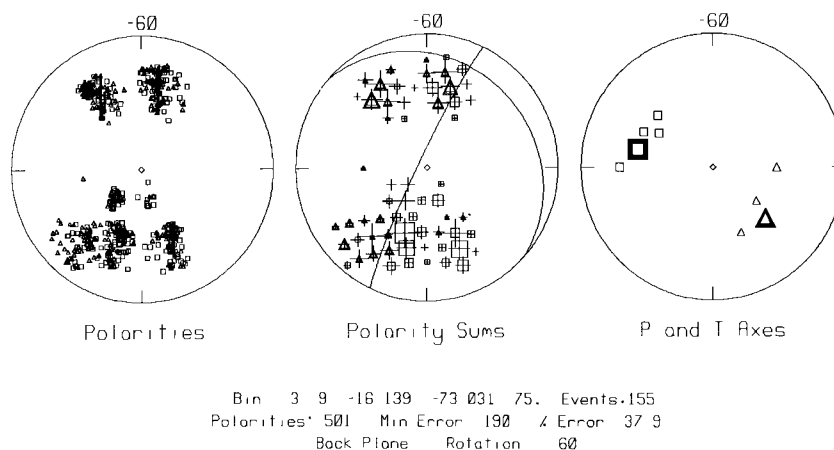

Fig. 5b

Polarities   Polarity Sums   P and T Axes

Bin   3   9   -16 139 -73 031   75.   Events.155
Polarities' 501   Min Error   190   % Error   37 9
Back Plane   Rotation   60

Fig. 6. Polarities, polarity sums, and focal mechanisms (P and T axes) for bin 3-9, as an example of the data reduction process. Projections are equal-area back planes looking toward N60W (parallel to the trench, to conform with Figure 7). A composite focal sphere of polarities is plotted at left with dilatations as squares and compressions as triangles. The polarity sum sphere (PSS) (center) depicts the net sums of compressions (+1) (triangles) and dilatations (−1) (squares), and number of polarities (crosses) within small nonoverlapping regions centered at 10° intervals on the focal sphere. All symbol heights are proportional to the square root of the sum. A solitary cross indicates a zero sum. The maximum-likelihood (or minimum-error) fault plane solution (right) is indicated by T (large square) and P (large triangle) axes, placed at the centers of their 10° averaging regions. The accompanying small symbols indicate the solution stability obtained by determining all solutions with an additional 1% error over the minimum-error solution (e.g., 37.9% for bin 3-9). The fault planes corresponding to the minimum-error solution are superposed on the PSS. Observe the trend in polarity sum distribution, with the nodal planes precisely dividing quadrants of dominant compression and dilatation.

and Bullen, 1958] used in the hypocenter-locating process [Boyd et al., 1984].

Focal Mechanism Determination

Numerous methods exist to detect dominant mechanisms from composite focal spheres. Our main interest is in resolving predominant orientations of stress axes and error bounds, regardless of the underlying variability of individual mechanisms [e.g., Dillinger et al., 1972; Brillinger et al., 1980; Hasegawa and Sacks; 1981]. For P wave polarities alone, and equal weighting of all readings, the maximum likelihood model of Brillinger et al. [1980] is satisfied by finding the fault plane solution(s) with the minimum number of inferred polarity errors [Dillinger et al., 1972; Brillinger et al., 1980]. Solutions with additional errors indicate solution stability, or a range of possible solutions [e.g., Dillinger, 1972; Hasegawa and Sacks, 1981].

We do a systematic search of the entire focal sphere to find the range of minimum-error solutions for each composite [Snoke et al., 1984]. We search the focal sphere at 5° increments in the B (null) and A (perpendicular to the fault plane) axes, solving for the number of inferred polarity errors in each case. When solving for a range of solutions, it is most useful to consider solutions as pairs of tension (T) and compression (P) axes. For each focal sphere composite we display the minimum-error solution(s), along with error bounds comprising all solutions with an additional ≥1% error (Figure 6) to indicate stability. In this way, solutions constrained by but a few observations will be identified.

Solution Stability and Polarity Sums

While errors in polarity readings can account for only 10-15% of the total error, the level of polarity errors in fault plane solutions varies from 16.3 to 37.9% (see Figure 7). It

is therefore evident that closely spaced events can vary in mechanism. We caution, however, that the significance of percent-minimum error and solution stability can be seriously affected by polarity distribution. This is illustrated most simply by considering the effect of clustering polarity data either near a P wave nodal zone or near a zone of dominant compression or dilatation. The near-nodal data will yield a relatively high minimum error but with very high stability when additional errors are allowed (e.g., bin 3–9 in Figure 7). On the other hand, clusters of data distant from a P wave node will yield a relatively low minimum error but with low stability as well (e.g., bin 9–9 in Figure 7). Thus error rates and stability should be considered qualitatively and not as probabilistic confidence levels. In the end, solution stability is to be evaluated in the context of the stress patterns observed across the W-B zone.

The range of observed polarity errors (or inconsistencies) can be explained by variations in focal mechanisms. A variation of as little as 30° in T and P axes can yield a 33% probable error in polarities, based on a uniform distribution of polarities across the focal sphere. Thus a mean error rate of 25–30% can in fact be explained with as little as 15° of variation in T and P axes, assuming 10–15% reading error. Moreover, our error rates are quite consistent with those found by Hasegawa and Sacks [1981] for composite solutions using primarily long-period teleseismic arrivals from the ISC catalog. Grange et al. [1984] also show substantial variation in single-event mechanisms calculated from closely spaced microearthquakes in this same region of southern Peru.

As a means of highlighting trends in the distribution of polarities on the focal sphere, we examine the data using polarity sum spheres. The focal hemisphere is divided into 224 nonoverlapping regions centered at approximately equal 10° spacings. Polarities are assigned +1 for compression
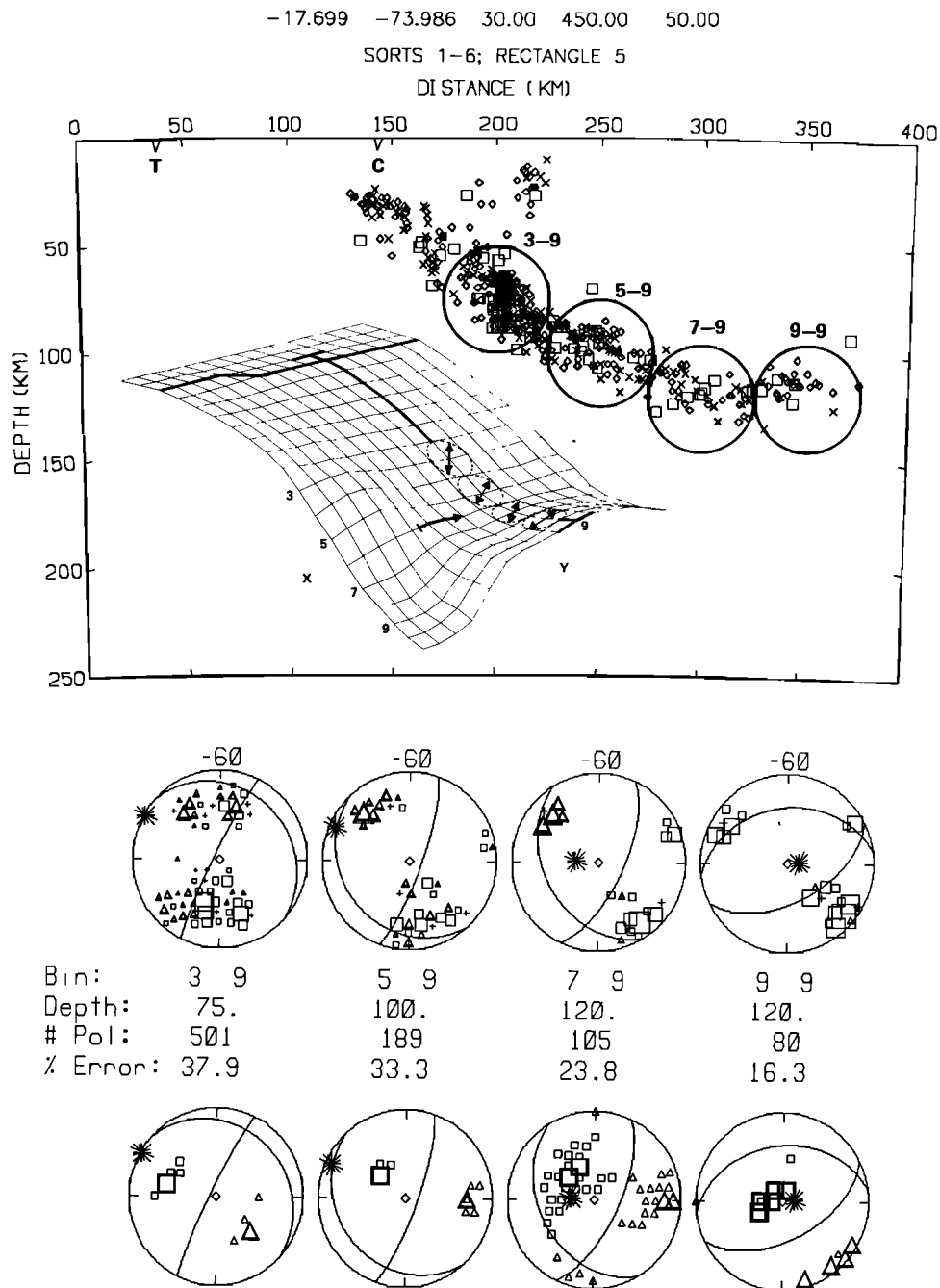
Fig. 7. Seismicity, polarity sums, and focal mechanisms for a seismicity section perpendicular to the trench strike (looking N60W) (section E, Figures 3 and 4). The inset surface indicates the projection angle (single-headed arrow), width of cross section (bracketed), and the in-plate orientation of the dominant T axis for each bin. T axes point essentially toward the contortion, initially pointing obliquely to the downdip axis, then rotating to parallel the trench within the concave zone 275–375 km from the trench. Projections of polarity sums (middle) and focal mechanisms (bottom) are back-plane projections viewed in the same direction as the seismicity cross section. The symbol convention is identical to Figure 6 with the exception that the cross indicates only the zero sum and not relative numbers of polarities. In addition, the asterisk indicates the local orientation of the downdip vector of the hypocenter surface.

and –1 for dilatation, then summed for each polarity region. A positive sum indicates dominant compression, and a negative sum dominant dilatation. The result is termed a polarity sum sphere (PSS), an example of which is shown in Figure 6. Symbols for compression (triangle) and dilatation (square) are scaled to reflect the magnitude (absolute value) of the sum. Regions of the focal sphere in the vicinity

of nodal planes yield small or zero sums, while regions far from nodal planes are dominantly positive or negative.

Polarity sum spheres are extremely useful for detecting patterns or complications in the polarity distribution, without making any assumptions about mechanism(s). In Figure 6 we see that although the error level in the fault plane solution for bin 3–9 is 37.9%, polarity sums cluster in re-
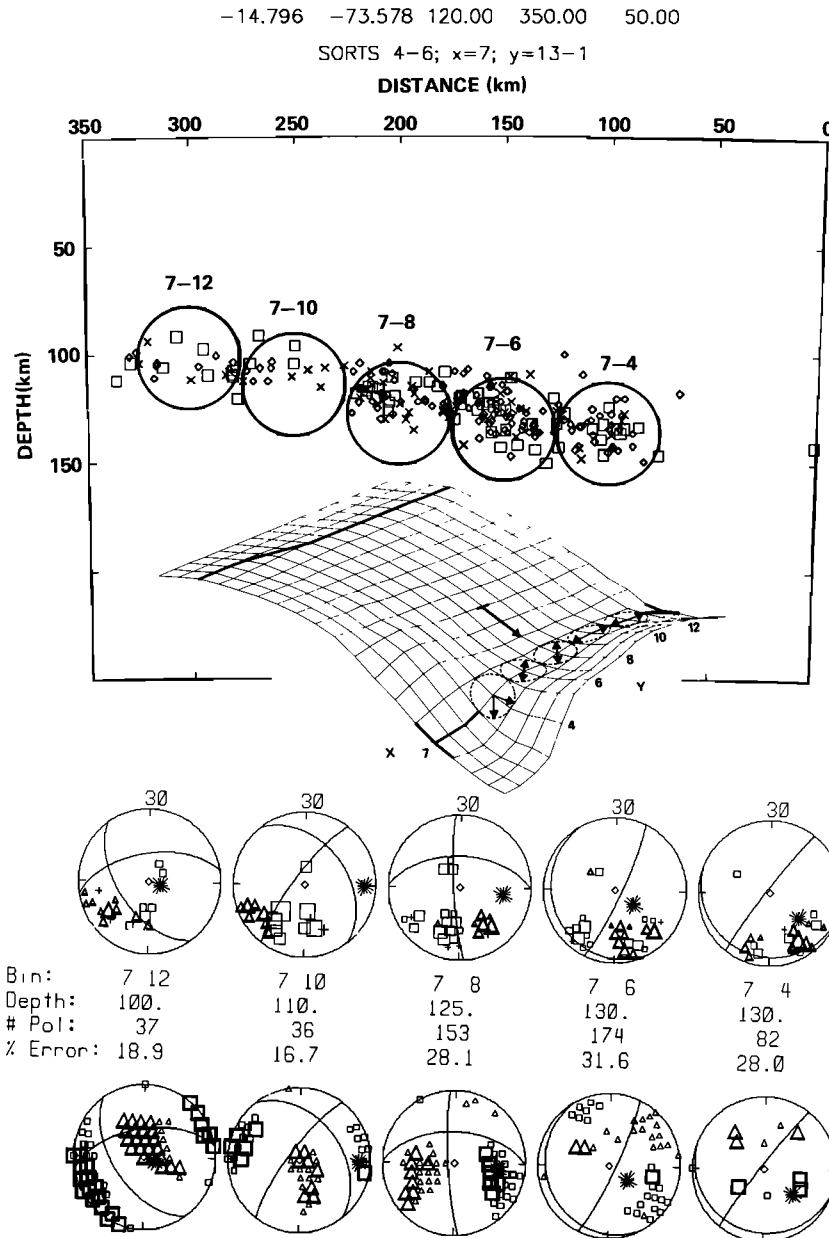
Fig. 8. Seismicity, polarity sums, and focal mechanisms for a seismicity section parallel to the trench strike (looking N30E) 275–325 km from the trench (sections A–G of Figure 4a). The absence of seismicity between 0 and 50 km along strike corresponds to an apparent increase in the degree of contortion (section A–B, Figure 4a). T axes are approximately parallel to the trench in the concave zone and rotate toward the contortion as the dip along the projection plane increases. The inset surface shows two dominant T axes for bin 7-4; this is evident from the T axes indicated in the lower right-hand focal mechanism solution.

gions of dominant compression and dilatation, corroborating the choice of fault planes. In fact, the higher percentage of errors near the nodal plane in the lower left quadrant is important for constraining the solution. We may also confirm changes or trends in apparent stress between adjacent event bins, independent of the resolution of focal mechanisms. This is apparent in Figure 7, where we see a progression of focal mechanism solutions for a cross section of seismicity. From polarity sums we observe complications in composites containing events from shallower than 50-km depth, indicating multiple mechanisms might be operating in any given averaging bin. These events are a combination of interplate thrust events, intracontinental plate events,

and complex intra-Nazca plate events [Sacks et al., 1978; Grange et al., 1984; Jordan et al., 1983]. Throughout the rest of the W-B zone, with the exception of a few transitional bins, each polarity sum distribution can generally be explained by a single dominant mechanism.

Focal Mechanism Solutions

We resolved dominant stress axes for all event bins centered at $\geq$75-km depth (Figure 5). As a means of displaying major trends in the data, we present three cross sections within the W-B zone at different projection angles. Figures 7–9 depict seismicity, polarity sums, and focal mechanism
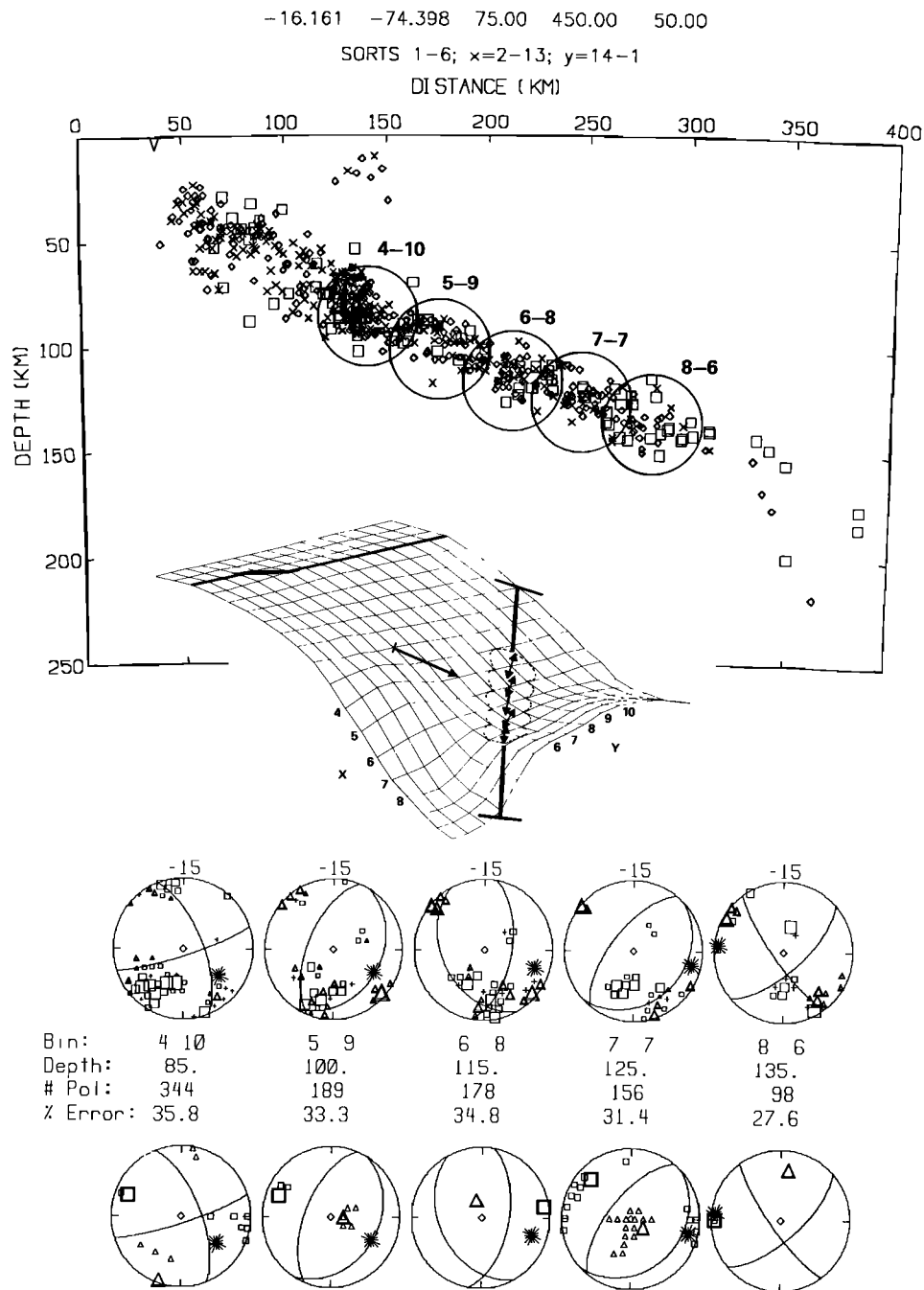
Fig. 9. Seismicity, polarity sums, and focal mechanisms for a seismicity section at 45° to the trench strike (looking N15W). Note the gradual decrease in dip angle (from left to right) with increasing distance from the trench and the sharp increase in dip just beyond bin 8-6. T axes are approximately in plate and parallel to the projection plane and hence pointing toward the contortion (N75E).

solutions for cross sections of seismicity taken perpendicular, parallel, and at 45° to the trench strike, respectively. These figures clearly illustrate that distributions of polarity sums (middle of figures) are consistent with minimum-error fault plane solutions.

Figure 7 exhibits a section of the W-B zone extending from the coast into the concave zone, perpendicular to the trench strike (section E, Figures 3 and 4). This figure shows a change in dominant mechanism across the seismic section. Note the pronounced tendency for the T axes to be within the seismicity plane and to point toward the contorted zone (near portion of contoured figure), rotating from nearly E-

W and oblique to the trench at the top of the zone (near the coast), to NW-SE and parallel to the trench in the concave zone. The change in polarity sums from dominant compression in the upper left quadrant of bin 7-9 to dilatations in the same region of bin 9-9 confirms the resolved rotation of stress axes. It is also apparent that there is more consistency in mechanisms for event bins deeper than about 100 km than there is for shallower events.

Figures 8 and 9 extend into the contortion. Figure 8 parallels the trench, extending from the concave to the convex zone (NW to SE). There is a general tendency for the T axes to parallel the trench within the concave zone (see
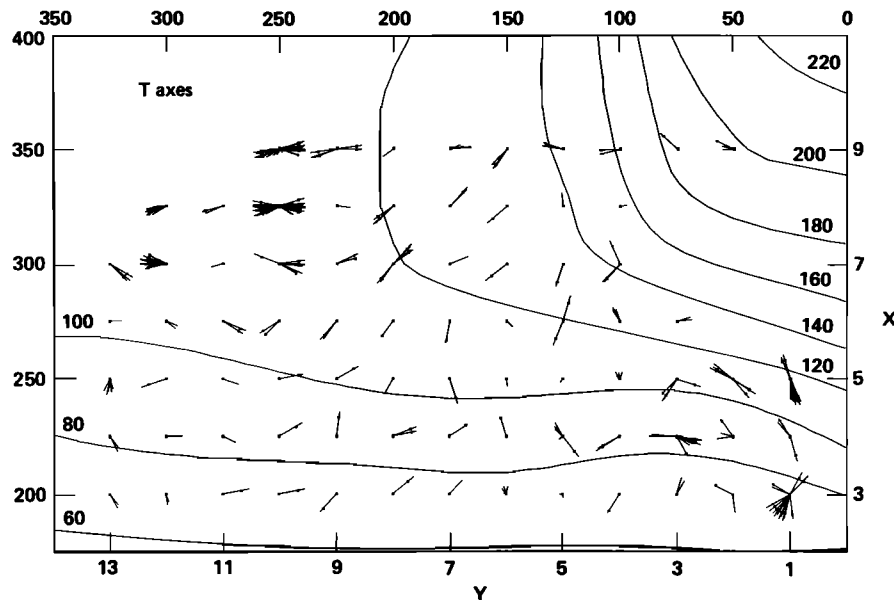
Fig. 10. Intraplate components of tension axes from minimum-error fault plane solutions superposed on seismicity-depth contours of the W-B zone beneath southern Peru. Lower hemisphere projections of minimum-error T and P axes (e.g., Figures 7-9) were rotated into the plane of the hypocentral surface (Figure 4b), then plotted relative to the epicenter of each event bin (Figure 5). Multiple solutions are indicated where more than one $10°$ averaging region contains a minimum-error T axis. Bin numbers x-y and distances perpendicular (x) and parallel (y) to the trench are keyed to Figure 4b. Axes within $30°$ of the local W-B zone surface are marked at $30°$ plunge. Although solution stability is not explicitly indicated, a sense of stability is perceived by looking at trends or variations in axes between adjacent (and overlapping) bins. For reference to previous figures, Figures 7 and 8 display mechanisms from alternating bins from 3-9 to 9-9 (perpendicular to trench) and from 7-12 to 7-4 (parallel to trench), respectively; Figure 9 displays an oblique section from 4-10 to 8-6.

inset surface) and to rotate toward the contortion as the contortion becomes more severe. A rotation in mechanism is clear from the change in juxtaposition of positive and negative polarity sums from the bottom of PSS 7-10 to the bottom of 7-8. This indicates that the T axis rotates along with the downdip vector, as observed in the focal mechanism solutions (bottom of figure). Figure 9 is an oblique cross section projected at 45° to the trench, from the coast to the contortion. T axes remain dominantly in plate and parallel to the projection plane along the entire traverse.

Local Stress Distribution

When fault plane solutions for all of the event bins in the vicinity of the contorted W-B zone are combined, a coherent stress pattern emerges. Figures 10 and 11 display the in-plate components of tension (T) and compression (P) axes, respectively, for composite focal spheres from 78 bins of hypocenters (Figure 5) in an area 200 by 350 km. We may expand on the discussion of trends made apparent in Figures 7-9, focussing mainly on T axis trends observed in Figure 10.

From 50- to 100-km depth ($x = 3, 5$) the stress pattern is complicated, but by no means incoherent. In this depth range there can still be some interaction between the subducting plate and the overlying continental lithosphere. Seismicity-depth contours are essentially parallel to the trench strike, and the W-B zone dip is uniformly ~30° (Figure 4). T axes in the northwest (lower left, $y = 10$, 13) section display the most uniform pattern, ranging from nearly parallel to trench strike (N120E) to pointing toward the contortion (N75E). In the middle zone ($y = 5, 9$), T

axes flip from pointing toward the contortion (N75E, $y = 7, 9$) to being nearly perpendicular to it (N, $y = 5, 6$). In the southeast (lower right, $y = 1, 4$), stress is particularly difficult to constrain, but there is a reorientation at $x = 4, 5$ and $y = 1, 2$ toward downdip tension (N10-30E). We caution that some of these complications may arise partly from the mixture of interplate and intraplate mechanisms. We note also that, in spite of the uniform shape of the W-B zone in this depth range, there are dramatic lateral changes in the level of seismicity in this zone. In particular, there is a high level of seismicity in the middle (transition) zone in this depth range (sections D and E, Figures 3 and 4), precisely where mechanisms are most variable.

From 100- to 140-km depth ($x = 6, 9$), T axes exhibit a very well-defined and coherent pattern. This area encompasses the NW concave zone and most of the contorted zone. Throughout this depth range, polarity-error rates are relatively low, averaging about 20%. In the far northwest section ($y = 10, 13$), the in-plate component of tension is dominantly parallel to the trench strike and points toward the contortion. In the middle section ($y = 5, 9$) there is a dramatic rotation in tension axes that conforms remarkably well with the change in surface gradient. In particular, along the 120-km depth contour, which rotates about 90° between the concave northwest section and the convex southeast section, T axes are everywhere perpendicular to the depth contour. In the southeast section, at depths greater than 140 km ($x = 1, 4$), mechanisms are not well constrained due to the paucity of events.

We can test the hypothesis that T and P axes tend to lie near the seismicity plane. For a uniform random distribution of T or P axes there is a 50% chance that each axis will
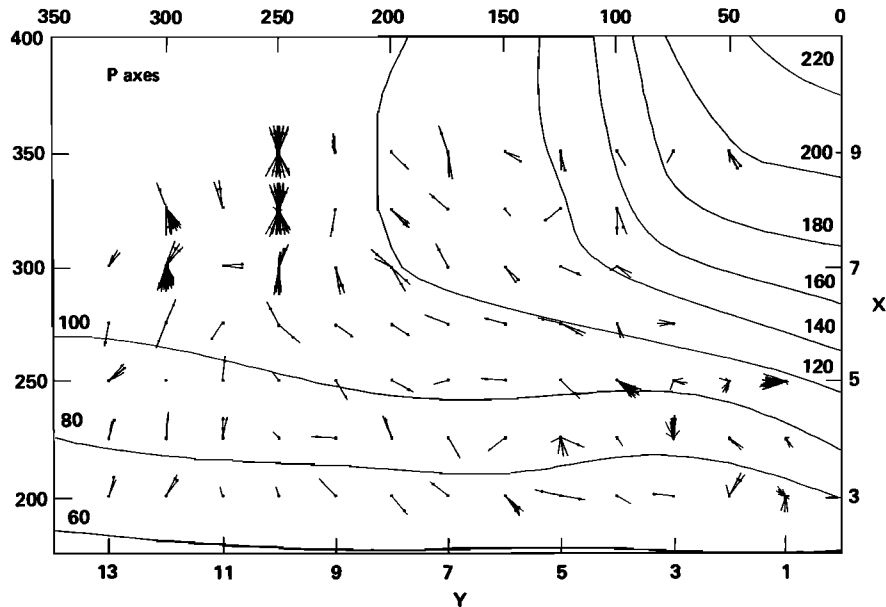
Fig. 11. Intraplate components of compression (P) axes from minimum-error fault plane solutions superposed on seismicity-depth contours of the W-B zone beneath southern Peru.

fall within 30° of any given plane. In Figures 10 and 11 a 30° plunge mark is indicated on those axes that are within 30° of the seismic plane. Overall, 60% of T and P axes are within 30° of the local plane, 30% are out of the plane, and 10% are indeterminant. Thus overall, both T and P tend to be in plate. Exceptions for T axes occur, for example, in mechanisms shallower than 120-km depth in the middle zone ($x = 3, 6; y = 4, 6$) and in the far NW ($y = 12, 13$). P axes tend to be out of plate at depths shallower than 100 km in the NW ($y = 10$) and SE ($y = 1, 3$). The major portion of both diagrams (i.e., $y = 7, 10$ shallower than 120 km and $y = 4, 10$ at greater depth) shows T and P almost exclusively in plate. We see no overall tendency for T axes to be constrained better than P axes, or vice versa. On this basis, we cannot conclude that either tension or compression is the controlling stress component in this region.

We summarize our view of the in-plate T axes in Figure 12. Axes display remarkable coherency throughout the NW section from the trench down into the flat lying zone, defining a fan shape that converges to the southeast within the contortion itself. The plate is clearly being extended in a fashion that suggests that the deepest part of the seismic zone, within the convex section to the SE, is sinking and pulling the more buoyant concave NW section. Moreover, the extension is evident 100–150 km distant from the region most severely contorted. T axes at depths shallower than 100 km and updip from the convex zone are somewhat more complicated but still exhibit a general tendency for normal, downdip tension. In this depth range a slight rotation in T axes is observed as one proceeds parallel to the trench from the middle of the zone to the SE end (middle to right), suggesting that the contortion exerts an influence on focal mechanisms throughout the 200 by 350 km zone.

DISCUSSION

Regional Stress Distribution

The focal mechanism studies of Stauder [1973, 1975] and Hasegawa and Sacks [1981] provide a general framework for

the regional stress pattern observed in intermediate-depth earthquakes in Peru and northern Chile. The W-B zone is essentially free of contortions for several hundred kilometers along strike to both the north and south of our study area in southern Peru [Bevis and Isacks, 1984] (Figure 1). In both of these regions, T axes are dominantly downdip and perpendicular to the trench. Stauder's and Hasegawa and Sacks' observations in southern Peru may also be placed in the context of our own localized model in the vicinity of the W-B zone contortion (Figure 12). We have projected in-plate T axes from Hasegawa and Sacks (sections D, E, F, and G of Figures 8, 10, and 11 of Hasegawa and Sacks) approximately at the centers of their averaging regions (Figure 12), which are ~100 km in diameter. We have also included the T axis of one of Stauder's single-event mechanisms (event 24, Figure 4 of Stauder), which occurred near the contortion. At 100–150 km along strike to the northwest and southeast of our study area, tension axes tend to point downdip and perpendicular to the trench, further corroborating the trends observed at greater ranges in central Peru and northern Chile.

Within our local study area, T axes from Hasegawa and Sacks are affected by the contortion in a pattern similar to our microearthquake observations. In the NW concave section we observe the same rotation of T axes toward the contortion determined from our local earthquakes. Within the SE convex section, the one composite available from above 100-km depth has a T axis oblique to the trench strike, perhaps reflecting the complex nature of mechanisms in this zone. Below 100-km depth, T axes are again downdip and perpendicular to the trench. Stauder's event occurred closest to the center of bin 5–7 and has a T axis within 10° of the local downdip direction. Although this solution is in agreement with the T axis trend from our study, our data (Figure 10) indicate that the stress pattern is not particularly stable in this zone. In general, however, the results from teleseismic observations are in remarkable accordance with our pattern of T axes.

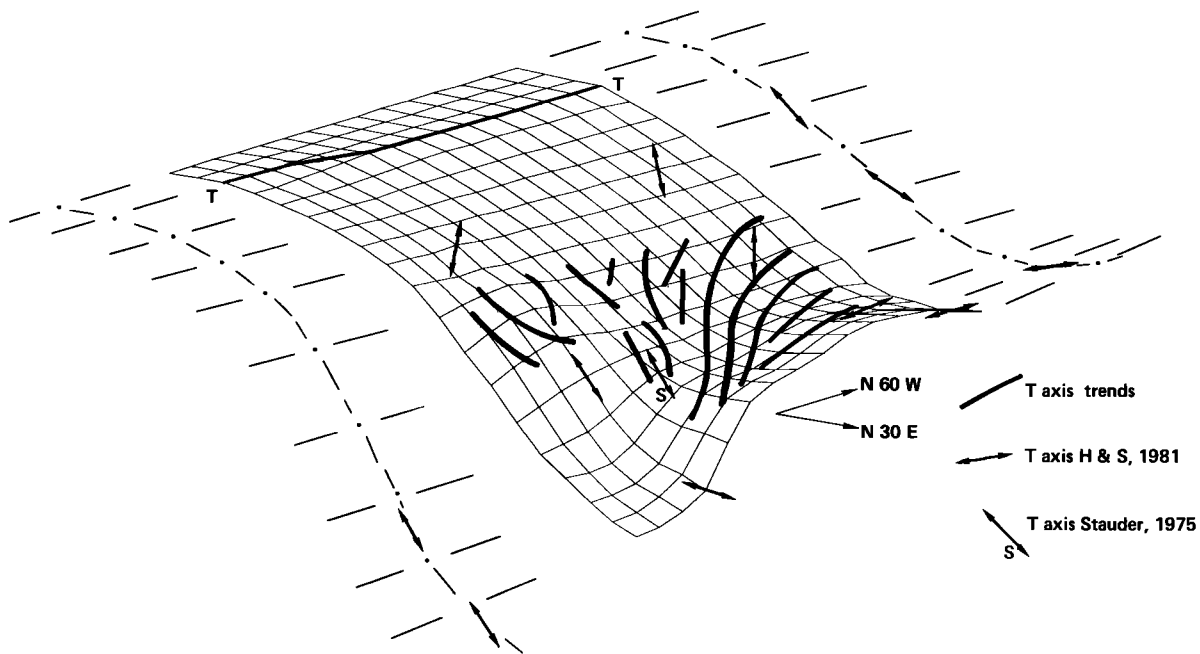It is evident that T axes tend to be downdip and perpen-

Fig. 12. Summary diagram of dominant in-plate tension (T) axes from this study compared with results of previous studies of teleseismic events. The heavy lines are smoothed contours of T axes of composite focal mechanisms of local microseismicity (derived from Figure 10). The short, double-ended arrows are from teleseismically determined composite mechanisms from *Hasegawa and Sacks* [1981] (sections D, E, F, and G), together with one single-event mechanism from *Stauder* [1975] (designated by "S"). The contours outside the local W-B zone are drawn assuming the general shape of the slab does not change appreciably along strike outside the region of this study.

dicular to the trench, except within 150 km of the contortion. Near the contortion we are able to separate the forces in the plate due to plate motion and subduction from those forces that produce the contortion. Here, T axes tend to be aligned with the local downdip vector and/or to point toward the contortion. The stress pattern is modified in a manner that suggests that significant plate extension occurs prior to actual physical manifestations of contortion. This is demonstrated very clearly by the fan-shaped trend in T axes (Figures 10 and 12), which tends to converge in the deepest zone of seismicity in the southeast corner of the study area. This implies that not only is a large portion of the plate being extended or pulled toward the deeper southeast zone, but also that the normal slab-pull force perpendicular to the trench is severely modified and/or dominated in the vicinity of the contortion.

We hypothesize that slab-pull forces dominate the expression of stress in the W-B zone beneath southern Peru. The slab-pull concept is also supported by the conclusions of *Sacks* [1983] that the transition in plate geometry between central and southern Peru (from concave to convex) is caused by differences in slab buoyancy. This would produce tension between the concave buoyant region and the convex region. Furthermore, *House and Jacob* [1983], in a study of intermediate-depth earthquakes beneath the Aleutian Islands, suggest that if interplate coupling is high at shallow depth, the resistance near the surface could enhance/induce net tensional stress in the downgoing plate as it is pulled downward by negative buoyancy. The interplate coupling along the Peru-Chile trench is presumably high [*Ruff and Kanamori*, 1983] due to the generally young age of subducting lithosphere (~50 m.y. at the trench; *Mammerickx et al.*, [1980]) and fast relative plate motion (10 cm/yr). Thus

the combination of interplate coupling at the trench and buoyancy of the concave zone in central and south-central Peru may be significant factors in the development of plate extension toward the contortion.

Other Stress Hypotheses

We may test the hypothesis that slab-pull forces dominate over other sources of stress in the contorted Nazca plate beneath southern Peru. Other possibilities include the effect of plate convergence direction, plate bending, or plate inextensibility.

Plate convergence. *Grange et al.* [1984] observed a primary axis of contortion in southern Peru that is aligned approximately parallel to the direction of relative plate motion, N80E. In their view, this alignment suggests that the contortion need not migrate with respect to the position of the overriding South American plate, in which case the flow in the surrounding asthenosphere would be in steady state. If this is so, then it indicates that the direction of plate motion, and hence the subduction angle at the trench, exerts a strong influence on both the plate shape and on the distribution of stress within the W-B zone.

We disagree with this interpretation. First of all, as mentioned previously, we do not observe a linear axis of contortion (e.g., Figures 10 and 11). Second, overwhelming evidence suggests that the stress pattern of intermediate-depth events, and hence plate geometry in this depth range, is not particularly influenced by the direction of relative plate motion. This is made evident by the fact that T axes outside the contorted zone are generally perpendicular to the trench, even as the trench orientation changes with respect to the direction of relative plate motion from Peru to north-
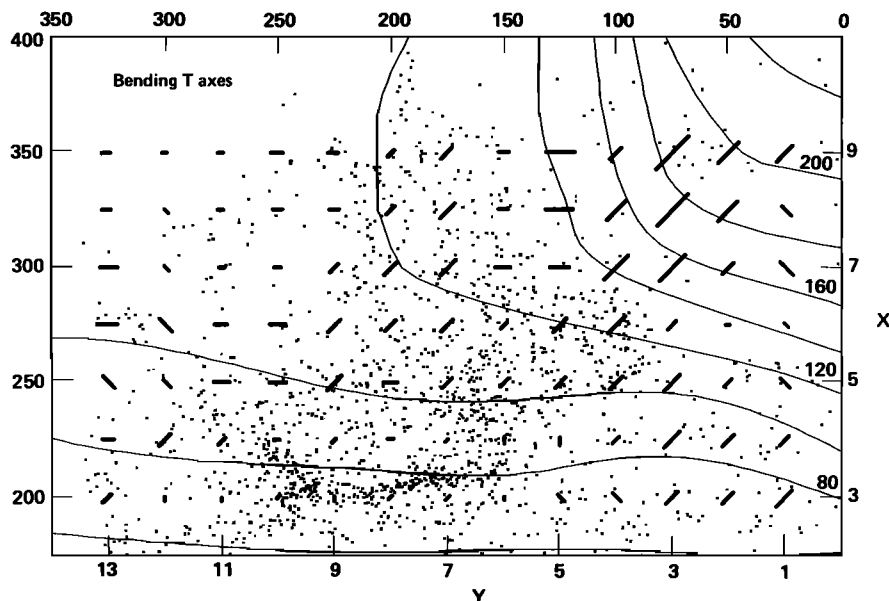
Fig. 13. Tensional bending stress and intermediate-depth seismicity in southern Peru. Where the dominant bending is convex, T axes are plotted with length proportional to the angle of bending. Where bending is concave, the corresponding P axis is rotated $90°$ to represent the equivalent T axis. The local seismicity is from depths ≥ 50 km.

ern Chile (Figure 1). This result is also observed between northern Honshu and Hokkaido [*Umino et al.*, 1984], where the Hokkaido corner exhibits a change in trench strike of $\sim 45°$ over a distance of 100 km. In particular, T axes at intermediate depth in the lower seismic plane rotate around the corner, remaining perpendicular to the trench and parallel to the local downdip direction.

Plate extensibility. The concept of plate extension is in conflict with the model of *Yamaoka et al.* [1986], which assumes that subducting plates are essentially elastic and inextensible. However, plate inextensibility requires that the plate beneath southern Peru must be either torn [e.g., *Barazangi and Isacks*, 1979] or severely folded over on itself — neither of which is supported by our data. Plate extension is further supported by theoretical considerations [*Bevis*, 1986]: an elastic, inextensible surface has a constant Gaussian curvature, defined by $1/(R_1 R_2)$, where R_1 and R_2 are the major and minor radii of curvature, respectively. The observed W-B zone shape does not satisfy this criterion. A cursory examination of the W-B zone fit given by *Yamaoka et al.* — constrained to the Gaussian curvature of a spherical shell of earth radius — versus our own fit to the hypocenter trend (Figure 4) suggests that 10% extension of the plate is indeed plausible.

Plate bending. Plate-bending stress has been proposed to explain much seismicity in subduction zones, especially double W-B zones [e.g., *Kawakatsu*, 1986]. Figure 13 exhibits the configuration of T axes for bending stress alone, based on our W-B zone model. Directions and magnitudes of maximum compression and tension were calculated from apparent changes of dip in the W-B zone model (Figure 4b) at 45° intervals in azimuth. For any given maximum stress, the opposing (90°) stress is generally very small. Comparison of T axes due to bending and those observed in focal mechanisms (Figure 10) shows clear similarities. There is a notable exception in the contortion, however: bins 9–2 to 9–4 have T axes nearly perpendicular to those inferred from bending stress. It is also notable that the level of

seismicity and degree of bending bear no particular relationship to one another (Figure 13). In fact, where bending is most severe in the contortion, the plate is nearly aseismic. Conversely, along the 80-km depth contour, bending is minimal, yet seismicity is high. The observed seismicity pattern is not an artifact of station geometry: *Grange et al.* [1984] observe a similar pattern of local seismicity from a very different array configuration. Thus although bending may contribute to seismicity in some areas, such as bins $x = 7, 9$ and $y = 6, 8$ in the transition zone, bending is generally not consistent with the seismicity pattern. Further evidence against bending is apparent in the composite mechanisms of *Hasegawa and Sacks* [1981] in central Peru. They find T axes universally downdip even as the plate-dip shallows to horizontal (composites B-4, C-3, and D-2 of *Hasegawa and Sacks*; rightmost profile Figure 11, this study). The concave upward profile of seismicity in this region indicates that the plate should be in compression perpendicular to the trench due to bending. Evidently, slab-pull dominates over bending.

These and other models have been proposed to explain the stress distribution observed from intermediate-depth and deep earthquakes. In addition to plate-bending stress, thermal stress [e.g., *House and Jacob*, 1982; *Goto et al.*, 1983, 1985; *Hamaguchi et al.*, 1983] has been proposed to explain the hypocentral trend and focal mechansims observed in double W-B zones. Shear failure in the plane of the W-B zone has been proposed as an explanation for patterns observed in compressional earthquakes in deep events beneath Tonga [*Giardini and Woodhouse*, 1984]. In a future paper, we will evaluate such models in the context of observed stress distributions in critical subduction zones. Our data do not, however, support these sources of stress as dominant factors in the stress distribution observed in southern Peru. It is likely that the relative importance of each of these mechanisms is controlled by the rheology. For instance, it may be that the in-plane-shear model is applicable only to deep seismic zones under compression, suggest-

ing that subducted plates may extend much more readily than they compress. Local stresses such as thermal and bending may dominate where the combination of plate density (proportional to age) and plate motion do not yield net tension or compression in the plate as it subducts [*Fujita and Kanamori*, 1981]. Slab-pull effects may dominate where there is young lithosphere that is relatively buoyant near the surface and/or is tightly coupled at the trench. As the plate becomes older, buoyancy and coupling decrease, and the temperature and/or bending effects observed in double W-B zones may prevail.

CONCLUSIONS

Further study is needed to differentiate between several possible subduction processes contributing to the observed stress pattern in W-B zone earthquakes. However, our results definitely suggest that slab-pull force is the major contributor to the stress pattern observed in southern Peru. We do not see direction of plate convergence, slab-bending stress, thermal stress, or shear failure parallel to the W-B zone as important in this region. Our results also indicate that plate extension of up to 10% may occur and that plates cannot be satisfactorily modeled as inextensible below 50- to 100-km depth.

REFERENCES

Barazangi, M., and B. Isacks, Spatial distribution of earthquakes and subduction of the Nazca plate beneath South America, *Geology*, *4*, 686–692, 1976.

Barazangi, M., and B. Isacks, Subduction of the Nazca plate beneath Peru: Evidence from spatial distribution of earthquakes, *Geophys. J. R. Astron. Soc.*, *57*, 537–555, 1979.

Bevis, M., On the curvature of Wadati-Benioff zones and the torsional rigidity of subducting plates, *Nature*, *323*, 52–53, 1986.

Bevis, M., and B. Isacks, Hypocentral trend surface analysis: Probing the geometry of Benioff zones, *J. Geophys. Res.*, *89*, 6153–6170, 1984.

Boyd, T., A. Snoke, I. S. Sacks, and A. Rodriguez, High resolution determination of the Benioff zone geometry beneath southern Peru, *Bull. Seismol. Soc. Am.*, *74*, 557–566, 1984.

Brillinger, D. R., A. Udias, and B. A. Bolt, A probability model for regional focal mechanism solutions, *Bull. Seismol. Soc. Am.*, *70*, 149–170, 1980.

Dillinger, W. H., S. T. Harding, and A. J. Pope, Determining maximum likelihood body wave focal plane solutions, *Geophys. J. R. Astron. Soc.*, *30*, 315–329, 1972.

Evernden, J. F., Identification of earthquakes and explosions by use of teleseismic data, *J. Geophys. Res.*, *74*, 3828–3856, 1969.

Flinn, E. A., Confidence regions and error determinations for seismic event location, *Rev. Geophys.*, *3*, 157–185, 1965.

Fujita, K., and H. Kanamori, Double seismic zones and stresses of intermediate-depth earthquakes, *Geophys. J. R. Astron. Soc.*, *66*, 131–156, 1981.

Giardini D., and J. H. Woodhouse, Deep seismicity and modes of deformation in Tonga subduction zone, *Nature*, *307*, 505–509, 1984.

Goto, K., H. Hamaguchi, and Z. Suzuki, Distribution of stress in descending plate in special reference to intermediate and deep-focus earthquakes, I, Characteristics of thermal stress distribution, *Tohoku Geophys. J.*, *29*, 81–105, 1983.

Goto, K., H. Hamaguchi, and Z. Suzuki, Earthquake generating stresses in a descending slab, *Tectonophysics*, *112*, 111–128, 1985.

Grange, F., D. Hatzfeld, P. Cunningham, P. Molnar, S. W. Roecker, G. Suarez, A. Rodriguez, and L. Ocola, Tectonic implications of the microearthquake seismicity and fault plane solutions in southern Peru and their tectonic implications, *J. Geophys. Res.*, *89*, 6139–6152, 1984.

Hamaguchi, H., K. Goto, and Z. Suzuki, Double-planed structure of intermediate-depth seismic zone and thermal stress in the descending plate, *J. Phys. Earth*, *31*, 329–347, 1983.

Hasegawa, A., and I. S. Sacks, Subduction of Nazca plate beneath Peru as determined by seismic observations, *J. Geophys. Res.*, *86*, 4971–4980, 1981.

House, L. S., and K. H. Jacob, Thermal stresses in subducting lithosphere can explain double Benioff zones, *Nature*, *295*, 587–589, 1982.

House, L. S., and K. H. Jacob, Earthquakes, plate subduction, and stress reversals in the eastern Aleutian Arc, *J. Geophys. Res.*, *88*, 9347–9373, 1983.

Isacks, B. L., and M. Barazangi, Geometry of Benioff zones: Lateral segmentation and downward bending of the subducted lithosphere, in *Island Arcs, Deep Sea Trenches, and Back-Arc Basins, Maurice Ewing Ser. 1*, edited by M. Talwani and W. C. Pitman III, pp. 99–114, AGU, Washington, D. C., 1977.

Isacks, B. L., and P. Molnar, Distribution of stresses in the descending lithosphere from a global survey of focal-mechanism solutions of mantle earthquakes, *Rev. Geophys.*, *9*, 103–174, 1971.

James, D. E., I. S. Sacks, E. Lazo L., and P. Aparicio G., On locating local earthquakes using small networks, *Bull. Seismol. Soc. Am.*, *59*, 1201–1212, 1969.

Jeffreys, H., K. E. Bullen, *Seismological Tables*, British Association for the Advancement of Science, Gray Milne Trust, Office of the British Association Burlington House, London, England, 1958.

Jordan, T. E., B. L. Isacks, R. W. Allmendiger, J. A. Brewer, V. A. Ramos, and C. J. Ando, Andean tectonics related to geometry of subducted Nazca plate, *Geol. Soc. Am. Bull.*, *94*, 341–361, 1983.

Kawakatsu, H., Double seismic zones: Kinematics, *J. Geophys. Res.*, *91*, 4811–4825, 1986.

Mammerickx, J., E. Herron, and L. Dorman, Evidence for two fossil spreading ridges in the southeast Pacific, *Geol. Soc. Am. Bull.*, *91*, 263–271, 1980.

McLaren, J. P. and C. Frohlich, Model calculations of regional network locations for earthquakes in subduction zones, *Bull. Seismol. Soc. Am.*, *75*, 397–414, 1985.

Minster, J. B., and T. H. Jordan, Present-day plate motions, *J. Geophys. Res.*, *83*, 5331–5354, 1978.

Ruff, L., and H. Kanamori, Seismic coupling and uncoupling of subduction zones, *Tectonophysics*, *99*, 99–117, 1983.

Sacks, I. S., Interrelationships between volcanism, seismicity and anelasticity in western South America, *Tectonophysics*, *37*, 131–139, 1977.

Sacks, I. S, The subduction of young lithosphere, *J. Geophys. Res.*, *88*, 3355–3366, 1983.

Sacks, I. S., A. Linde, A. Rodriguez B., and J. Arthur Snoke, Shallow seismicity in subduction zones, *Geophys. Res. Lett.*, *5*, 901–903, 1978.

Snoke, J. A., I. S. Sacks, and H. Okada, Determination of subducting lithosphere boundary by use of converted phases, *Bull. Seismol. Soc. Am.*, *67*, 1051–1060, 1977.

Snoke, J. A., I. S. Sacks, and D. E. James, Subductions beneath western South America: Evidence from converted phases, *Geophys. J. R. Astron. Soc.*, *59*, 219–225, 1979.

Snoke, J. A., J. W. Munsey, A. G. Teague, and G. A. Bollinger, A program for focal mechanism determination of combined use of

polarity and SV-P amplitude ratio data (abstract), *Earthquake Notes*, *55*(3), 15, 1984.

Stauder, W., Mechanism and spatial distribution of Chilean earthquakes with relation to subduction of the oceanic plate, *J. Geophys. Res.*, *78*, 5033-5061, 1973.

Stauder, W., Subduction of the Nazca plate under Peru as evidenced by focal mechanisms and by seismicity, *J. Geophys. Res.*, *80*, 1053-1064, 1975.

Umino, N., A. Hasegaswa, A. Takagi, S. Suzuki, Y. Motoya, S. Kameya, K. Tanaka, and Y. Sawada, Focal mechanisms of intermediate-depth earthquakes beneath Hokkaido and northern Honshu, Japan, *Zisin*, *37*, 523-538, 1984.

Vassiliou, M. S., The state of stress in subducting slabs as revealed by earthquakes analysed by moment tensor inversion, *Earth Planet. Sci. Lett.*, *69*, 195-202, 1984.

Yamaoka, K., Y. Fukao, and M. Kumazawa, Spherical shell tectonics: Effects of sphericity and inextensibility on the geometry of the descending lithosphere, *Rev. Geophys.*, *24*, 27-53, 1986.

J. F. Schneider and I. S. Sacks, Department of Terrestrial Magnetism, Carnegie Institution of Washington, 5241 Broad Branch Road, N.W., Washington, DC 20015.